Research Article | Vol. 31, No. 21 / 9 Oct 2023 / Optics Express 33898
Optics EXPRESS

Simultaneous detection of greenhouse gases CH_4 and CO_2 based on a dual differential photoacoustic spectroscopy system

FUPENG WANG,[1,2,*] JINGHUA WU,[1] YAOPENG CHENG,[1] LIYAN FU,[1] JIANGUO ZHANG,[1] AND QIANG WANG[2]

[1] *Faculty of Information Science and Engineering, Engineering Research Center of Advanced Marine Physical Instruments and Equipment (Ministry of Education), Optics and Optoelectronics Laboratory (Qingdao Key Laboratory), Ocean University of China, Qingdao 266100, China*
[2] *State Key Laboratory of Applied Optics, Changchun Institute of Optics, Fine Mechanics and Physics, Chinese Academy of Sciences, Changchun 130033, China*
[*] *wfp@ouc.edu.cn*

Abstract: In addition to the atmospheric measurement, detection of dissolved carbon oxides and hydrocarbons in a water region is also an important aspect of greenhouse gas monitoring, such as CH_4 and CO_2. The first step of measuring dissolved gases is the separation process of water and gases. However, slow degassing efficiency is a big challenge which requires the gas detection technology itself with low gas consumption. Photoacoustic spectroscopy (PAS) is a good choice with advantages of high sensitivity, low gas consumption, and zero background, which has been rapidly developed in recent years and is expected to be applied in the field of dissolved gas detection. In this study, a miniaturized differential photoacoustic cell with a volume of 7.9 mL is designed for CH_4 and CO_2 detection, and a dual differential method with four microphones is proposed to enhance the photoacoustic signal. What we believe to be a new method increases photoacoustic signal by 4 times and improves the signal to noise ratio (SNR) over 10 times compared with the conventional single-microphone mode. Two distributed feedback (DFB) lasers at 1651 nm and 2004nm are employed to construct the PAS system for CH_4 and CO_2 detection respectively. Wavelength modulation spectroscopy (WMS) and 2nd harmonic demodulation techniques are applied to further improve the SNR. As a result, sensitivity of 0.44 ppm and 7.39 ppm for CH_4 and CO_2 are achieved respectively with an integration time of 10 s. Allan deviation analysis indicates that the sensitivity can be further improved to 42 ppb (NNEA=4.7×10^{-10}cm^{-1}WHz$^{-1/2}$) for CH_4 and 0.86 ppm (NNEA=5.3×10^{-10}cm^{-1}WHz$^{-1/2}$) for CO_2 when the integration time is extended to 1000 s.

1. Introduction

The Intergovernmental Panel on Climate Change (IPCC), an international body of the United Nations to advance scientific knowledge about climate change caused by human activities, gives a report that the global average surface temperature has increased by 0.6 ± 0.2 K since the late 19th century [1]. The IPCC concludes that "there is new and stronger evidence that most of the warming observed over the last 50 years is attributable to human activities". Methane and carbon dioxide (CH_4 and CO_2) are responsible for the majority of the Earth's greenhouse effect, atmospheric mixing ratios of CH_4 and CO_2 have been rising since the industrial revolution. So far, the atmospheric CH_4 concentration has almost doubled, and CO_2 concentration has increased about 35% since pre-industrial times at an average rate of 1-3 ppm .yr^{-1}. CH_4 is a potent greenhouse gas that contributes about 20% to the global warming induced by greenhouse effect [2]. An important fraction of CH_4 emissions comes from natural sources, which is estimated that natural ecosystems emit approximately 160 Tg . yr^{-1}. Within these emissions, it is estimated

#503454 https://doi.org/10.1364/OE.503454
Journal © 2023 Received 17 Aug 2023; revised 6 Sep 2023; accepted 6 Sep 2023; published 25 Sep 2023

Optics EXPRESS

that lakes and reservoirs emit about 92 $Tg.yr^{-1}$ [3–5]. CH_4 emissions from lakes and reservoirs depend on numerous processes involved in biogeochemical carbon cycling. For example, the balance of CH_4 production by methanogens and CH_4 oxidation by methanotrophs, such two major counteractive processes, strongly control the dissolved CH_4 concentrations in lake and reservoir water. Concentration of CH_4 in lakes and reservoirs water usually ranges from 1×10^{-8} to 3×10^{-3} mol/L [6]. This is higher than the concentration of CH_4 in atmosphere, which varies between 2.6×10^{-9} and 4×10^{-9} mol/L. Quantification of dissolved CH_4 concentration throughout the water column is an important step in understanding the complexity of CH_4 cycling in freshwater ecosystems, which ultimately allows the quantification of total diffusive CH_4 emissions to the atmosphere or can be used as a pollution indicator. As to CO_2, the determination of dissolved CO_2 is equally important, even if CO_2 emissions from freshwater ecosystems are usually lower compared with CH_4. The CO_2 is a central molecule of the carbon cycle, since it is the product of most biogeochemical processes, both aerobic and anaerobic, and the carbon source of several autotrophic processes, including primary production. Additionally, the CO_2 concentration combined with other parameters, gives valuable information about bioprocesses occurring in an ecosystem. In addition to the aforementioned research of global climate change, biogeochemistry and global carbon cycling, detection of dissolved CH_4 and CO_2 also plays a significant role in fields such as artificial carbon sequestration and marine resource exploration. As the increase of CO_2 concentration in the earth atmosphere, experts agree with that one promising approach for the reduction of the CO_2 amount entering the atmosphere is the storage of CO_2 in deep sea and deep underground, during which the dissolved gas sensing technique is required. Recent years, combustible ice has been found in high altitude frozen plateaus as well as underwater in marine sediments, whose main component is CH_4 [7]. In areas of combustible ice enrichment, the concentrations of CH_4 and CO_2 are often higher than regular level. Therefore, precise CH_4 and CO_2 sensing technology is also helpful for gas hydrate exploration and extraction [8].

Many methods have been developed to measure dissolved CH_4 and CO_2 since the early 1960s [9]. Due to the fact that gases are often poorly soluble in water and most gases are easier to detect in the gas phase than dissolved in liquids, the first step to detection is a gas-liquid separation process. After the dissolved molecule has been transferred to the gas phase, several detection methods can be used to measure its concentration, including gas chromatography [9,10], mass spectrometry [11,12] and laser spectroscopy based techniques [13–17]. Recently, significant advances have been made in the field of in-situ measurement of dissolved gases, combining membrane-based degassing technology and tunable diode laser absorption spectroscopy (TDLAS). In 2014, in-situ measurement of dissolved CH_4 and CO_2 in freshwater ecosystems was realized by an off-axis integrated cavity output spectrometer (OA-ICOS), detection limits of 2.76×10^{-10} mol/L for CH_4 and 1.5×10^{-7} mol/L for CO_2 were achieved [16]. These detection limits are below saturated concentrations with respect to the atmosphere and significantly lower than the minimum concentrations previously reported in lakes. In 2019, Li et al. developed a compact TDLAS-based system aiming for continuous measurement of dissolved CO_2 in seawater. Absorption line of CO_2 at 2004nm was selected, measurement precision of 4.18 ppm was achieved by virtue of a 2.86 m absorption cell at an integration time of 88 s [14]. In the same year of 2019, Liu et al. developed a similar system by replacing the 2004nm distributed feedback (DFB) laser with a 4319 nm interband cascade laser (ICL), and replacing the 2.86 m absorption cell with a 29.8 m one. Benefiting from the higher absorption line strength in the mid-infrared region (MIR) and longer absorption path length, the detection limit of CO_2 was improved to 0.72 ppb at an averaging time of 2 s [18]. Afterwards in 2020, the system was integrated and applied to the South China Sea for dissolved CO_2 analysis [17]. Another potential technology is cavity ringdown spectroscopy (CRDS), which can further improve the gas detection sensitivity by extending absorption path length to kilometers scale. In 2008, Picarro company developed a CRDS-based

Optics EXPRESS

analyzer which already had capabilities of measuring atmospheric levels of CH_4, CO_2 and H_2O [13]. Afterwards, the team from University of Southern Mississippi measured dissolved CH_4 by headspace equilibrating method with CRDS system, low nanomolar of CH_4 concentration can be detected with high reproducibility [19]. Very recently, researchers from China reported their studies about dissolved CH_4 and CO_2 based on their independently developed CRDS system. Outdoor in-situ measurement experiments were performed near the coast of Sanya Institute of Deep Sea of Hainan Province [20,21]. In a short summary, direct absorption spectroscopy-based techniques have been extensively developed for dissolved gases detection due to the advantages of high sensitivity and selectivity. However, they have the same limitation of a slow response. In order to improve the detection sensitivity, multi-pass long-optical-path gas cells and ring-down cavities are usually used in TDLAS and CRDS systems, which inevitably results in a large gas cell volume so that we have to extract more gas from liquid to fill the gas cell. However, slow degassing efficiency is a big problem which means the degassing process is time consuming. This is the reason why the response time of commercially available dissolved gas instruments ranges from a few minutes to tens of minutes [14]. Therefore, new technologies are expected to minimize gas consumption without compromising detection sensitivity.

Photoacoustic spectroscopy (PAS) is a good choice with advantages of high sensitivity, low gas consumption, and zero background, which has been rapidly developing in recent years and is expected to be applied in the field of dissolved gas detection [22]. The PAS system measures the acoustic signal generated from photoacoustic effect to retrieve the gas concentration, which greatly decreases the dependence on the absorption path length. To utilize its advantage of low gas consumption, PAS-based systems have already been widely applied to the detection of dissolved gases in transformer oil [23–26]. In a recently published study, a T-type photoacoustic cell with volume of 30 mL was designed to measure the dissolved acetylene gas in oil [26]. In addition to the microphone, quartz tuning fork (QTF) was also used to measure the absorption signal based on photoacoustic and photothermal effect in the quartz enhanced photoacoustic spectroscopy (QEPAS) [27] and light-induced thermoelastic spectroscopy (LITES) [28–30] systems. The QTF is not only small in size, but also has a high resonance frequency which is beneficial for designing very short acoustic resonators to realize standing wave. As a result of the tiny dimension of QTF and resonators, the PA cell volume can be easily reduced to a milliliter level. For example, Zheng et al. developed a near-infrared (NIR) QEPAS sensor based on a 28 kHz QTF, in which the QTF, acoustic micro resonator, gas cell and laser fiber were integrated within a super compact space [31]. Afterwards in 2023, Wang et al. developed a sub-mL photoacoustic gas sensor based on QEPAS to measure the dissolved CH_4 at the Haima Cold Spring Area in the South China sea [32]. An inner size of 12 mm $\times$ 6 mm $\times$ 4 mm was achieved to reduce the total gas consumption of less than 0.3 mL. Although QEPAS has an absolute advantage in miniaturizing the gas cell, however, bare QTF are easily affected by factors such as condensation of water vapor, dust, and corrosion from acid gas, as a result, the Q-factor and response efficiency of QTF would drift in a long-term [33].

In this study, we used commercial electric microphones instead of QTF to measure the photoacoustic signal to avoid the interference as mentioned above. Because the long-term stability of electric microphones has been widely verified in the consumer electronics industry. Meanwhile, we also made efforts to reducing the volume of photoacoustic cell. As a result, a differential photoacoustic cell with volume of only 7.9 mL was designed and manufactured. Considering that differential detection has been widely applied to PAS-based systems [34–36], we went a step further in this study that a dual differential strategy was proposed based on four microphones, named dual differential photoacoustic spectroscopy (DD-PAS), realizing 4 times photoacoustic enhancement compared with conventional single-microphone mode [37]. In addition, the broadband frequency response and low-Q characteristic of the photoacoustic cell give us opportunity to use frequency division multiplexing (FDM) technique for multiple gases

Optics EXPRESS

detection. To realize simultaneous detection of CH_4 and CO_2 gas, two DFB lasers operating at 1651 nm and 2004nm were chosen and driven in FDM mode. Wavelength modulation spectroscopy (WMS) and 2nd harmonic demodulation technique are applied to further improve the signal to noise ratio (SNR). The photoacoustic enhancement performance of DD-PAS, detection sensitivity of CH_4 and CO_2 were evaluated in detail by experiments.

2. Method

2.1. Absorption line analysis and laser sources selection

The dual gas sensor developed in this study is expected to be applied for dissolved CH_4 and CO_2 detection ultimately. High-concentration water vapor would inevitably enter the photoacoustic cell after the gas-liquid separation process. So, absorption interference from water molecule is considered when selecting the absorption line for CH_4 and CO_2 detection as depicted in Fig. 1. As simulated in Fig. 1(a), 1.8 ppm CH_4, 0.2% CO_2 and 2% water vapor are simulated in the same wavelength range from 1650 nm to 1658 nm. 1650.96 nm and 1653.72 nm are two good choices for CH_4 detection, among which the 1650.96 nm is the better one with less interference from water vapor. The CO_2 gas has absorption spectra in both the NIR and MIR regions, such as 1573 nm, 2004nm, 2051nm, 2672 nm, 4.3 μm and so on. The laser sources whose operating wavelength near 1573 nm and 2004nm are cheaper and easier to obtain and can be used for CO_2 measurements. However, the absorption line strength at 2004nm is stronger than that at 1573 nm by nearly two orders. So, the absorption spectrum of CO_2 from 2000nm to 2005nm are simulated as shown in Fig. 1(b), 2% H_2O and 0.1% CH_4 are simulated in the same region to analysis the cross-interference. The results indicate that 2003.5 nm is a good choice to sense the CO_2 absorption, meanwhile the interference from H_2O and CH_4 is reduced to the lowest level. Therefore, DFB lasers with wavelength of 1651 nm (DFB1651, OptoChip Photonics, China) and 2004nm (DFB2004, Nanoplus, Germany) are used in our experiments, the maximum output optical power is 60 mW at 320 mA driving current for DFB1651, and 10 mW at 140 mA driving current for DFB2004.

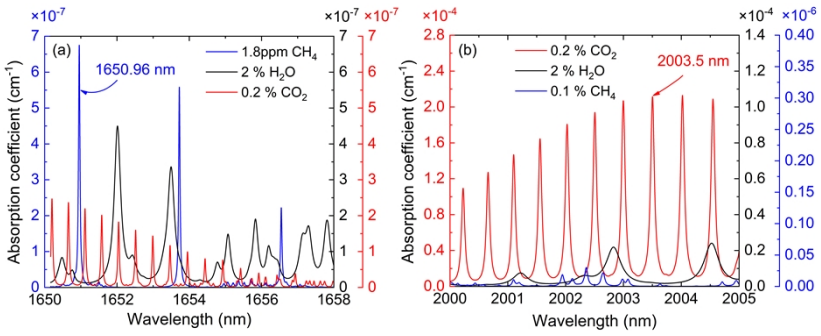

Fig. 1. Simulated absorption coefficient based on HITRAN database at 1 bar and 296 K. (a) Absorption coefficient of 1.8 ppm CH_4, 2% H_2O and 0.2% CO_2 in the wavelength band from 1650 nm to 1658 nm, (b) Absorption coefficient of 0.2% CO_2, 2% H_2O, and 0.1% CH_4 in the wavelength band from 2000nm to 2005nm,

2.2. Simulation of differential photoacoustic cell

Differential PA cells have been widely used in PAS-based gas sensing system due to its rejection of common-mode noises such as flow noise, window-absorption-induced noise and external electromagnetic or acoustic disturbances [38,39]. To apply such differential PA cell to dissolved gas detection, what we need to do is compressing the inner volume of such PA cell. We use finite

Optics EXPRESS

element analysis (FEA) to simulate the acoustic field distribution inside the PA cell via COMSOL software, the thermos viscous acoustics model is adopted in the simulation whereby both viscous and thermal surface loss are included. To simulate the absorption of laser irradiation by gas, a uniformly distributed heat source is set at the center of one resonator with an amplitude of 0.348 W/m^3. As shown in Fig. 2(a), the differential photoacoustic cell has a fully symmetrical configuration, composed of two identical cylinders served as acoustic resonators and two same cylindrical buffer chambers located at both ends. The radius and length of each resonator are optimized to 3 mm and 50 mm respectively, while the radius and length of two buffer chambers are optimized to 9 mm and 10 mm respectively, leading to an extremely small inner volume of ~7.9 mL. The acoustic field distribution at resonant frequency is depicted in Fig. 2(a). In this resonance mode, the antinodes of the acoustic waves are in the middle of two resonators and the maximum sound pressure is 1.375×10^{-5} Pa. Furthermore, as illustrated in Fig. 2(b), the frequency response of the differential photoacoustic cell is calculated, according to which the resonant frequency is determined to be 3124 Hz and the full width at half maximum (FWHM) of frequency response curve is obtained to be 98 Hz, resulting in a Q-factor of 31.9. The phase-frequency characteristic is displayed in Fig. 2(c), it is obvious that acoustic signals measured by two microphones differ by π in phase and this is the principle why differential detection here can double the photoacoustic amplitude. Finally, the cell constant is evaluated to be 2548 Pa/(cm^{-1} · W).

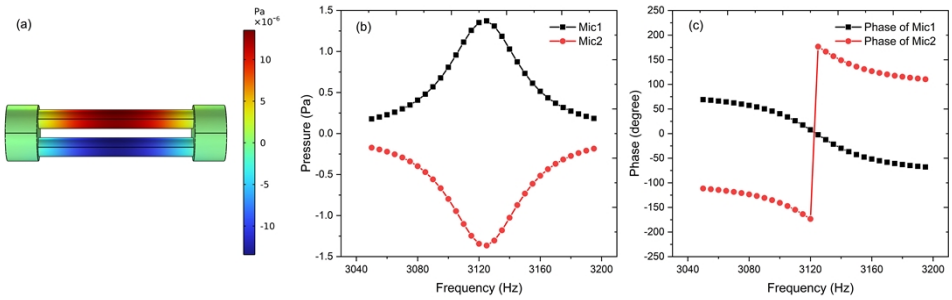

Fig. 2. FEM simulation results of the DPAC; (a) acoustic filed distribution at resonant frequency, (b) sound pressure frequency response of two resonators, (c) Phase-frequency characteristic of two resonators.

2.3. Manufacture of the dual differential photoacoustic cell

Based on the inner size of PA resonators and buffer chambers as simulated in the above, a 3D model is designed by SolidWorks software for manufacturing. As shown in Fig. 3(a), the PA cell has a fully symmetrical configuration, composed of two identical cylinders served as acoustic resonators (in red color) and two same cylindrical buffer chambers (in blue color) located at both ends. The critical dimensions have been marked in Fig. 3(b) in unit of millimeter. The assembly process is displayed in Fig. 3(c), two GaF_2 windows with diameter of 25 mm are mounted to allow the laser beam into the resonators, double O-rings are used to ensure air tightness. The physical image of the assembled PA cell is displayed in Fig. 3(d), material used for cell manufacturing is 316 L stainless steel.

Compared with previous differential PA cell where two microphones were used to detect the photoacoustic signal, the PA cell designed in this study used four microphones to realize the dual differential function for SNR improvement. Referencing the Fig. 3(a, b), acoustic standing waves, opposite in phase at resonance frequency, would form inside two resonators. Two pairs of electret condenser microphones (Mic-1 and Mic-2, Mic-3 and Mic-4) were positioned at the middle of each resonator. The first step is the same with the previous differential PA cell, differential operation is performed between Mic-1 and Mic-2, Mic-3 and Mic-4 to get diff-1 and diff-2, based

Optics EXPRESS

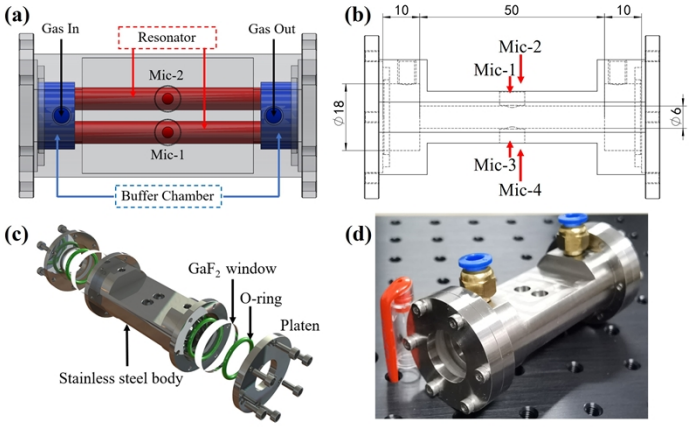

Fig. 3. Design and assembly of the dual differential photoacoustic cell. (a) Front view of the engineering model, (b) Bottom view drawing sheet, (c) Components assembly diagram, (d) Physical image of the photoacoustic cell.

on which the coherent noise components, such as flow noise, window-absorption-induced noise and external electromagnetic or acoustic disturbances, would be effectively suppressed, and in the meanwhile, the photoacoustic signals are doubled. In the past, only diff-1 was used for harmonic detection and gas concentration calculation. However, diff-1 and diff-2 were added in this study to further increase the photoacoustic signal. To our expectation, the photoacoustic signal would be increased by four times compared with the signal of single microphone, meanwhile the noise level would not worsen too much by the adding process. In brief of the dual differential method, common-mode noise is eliminated by the differential operation and dual-diff adding further increases the photoacoustic amplitude. This is different to simple accumulation of four microphones' signals.

3. Experiment system setup

In this section, an experiment system was constructed to serve this study. The core part of the experiment system is the photoacoustic excitation and detection module as displayed in Fig. 4, the PA cell is fixed to an optical breadboard through a 3D-printed base. Two DFB lasers operating at 1651 nm and 2004nm are employed to probe the CH_4 and CO_2 absorption line at 1650.96 nm and 2003.5 nm, laser beams are led to resonator-1 and resonator-2 of PA cell by two fiber collimators respectively for photoacoustic excitation. Two fiber collimators are mounted to the 3D-printed units as well. Two identical circuit boards designed by ourselves are used to measure the output signal of each microphone and perform the differential operation. The gain of each microphone's signal is set 50 times, and the differential gain is set 0 dB. To compare each microphone's signal and evaluate the differential performance, three signal output interfaces are set on each circuit boards as shown in Fig. 4(b), including the signal output of each microphone and the differential output, each of them can be connected to lock-in amplifier for harmonic detection. All the units as shown in Fig. 4(a, b) are integrated together to ensure the structure stability, and the entire module is placed in a soundproof cabin to further reduce the interference from external noise.

The working principle of the entire experiment system is illustrated in the schematic below. A commercial data acquisition (DAQ) card NI USB-6361 is employed for signal generation, data collection and processing, driven by a PC-based LabView platform. Sawtooth wave in frequency of 0.1 Hz and sine wave in high frequency (half of the resonant frequency of PA cell) are generated by the DAQ card and added to drive the DFB lasers by the laser controller. In

Optics EXPRESS

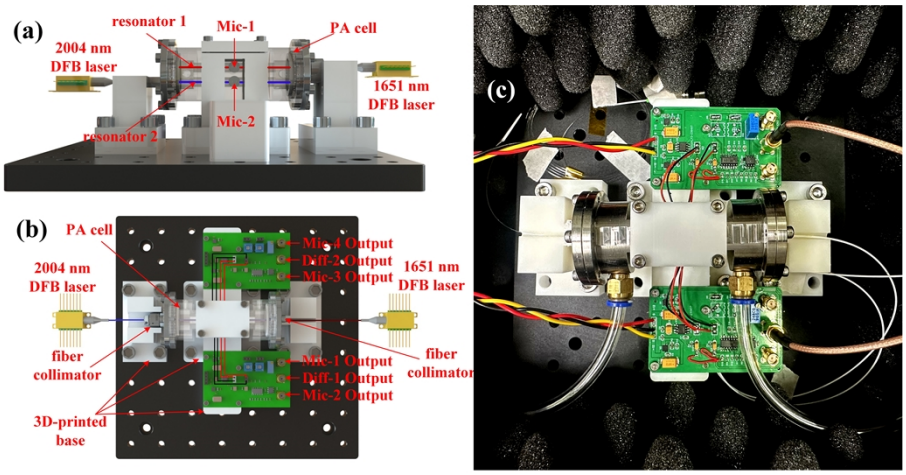

Fig. 4. The photoacoustic excitation and detection module. (a) Side view of the module, (b) Vertical view of the module, (c) The physical image of the photoacoustic module.

this study, two laser controllers, including a commercial instrument LDC501 and a homemade one [40], are used to stabilize the inner temperature of two DFB lasers and convert the driving voltage into current. Both DFB lasers operate in the wavelength scanning-modulation mode, the wavelength scanning is used to make the wavelength output cover the absorption lines of CH_4 and CO_2, the wavelength modulation is used to generate the absorption-induced harmonics. Laser beams pass through the resonators by fiber collimators as demonstrated in Fig. 4(a) to excite photoacoustic signal, which is measured by four microphones as explained above. The effective optical power for PA excitation at CH_4 and CO_2 absorption center is estimated to be 30 mW and 5 mW respectively. The signal output of circuit boards is collected by the analog-to-digital converter (ADC) of the DAQ card with a sampling rate of 2 MS/s, afterwards a self-developed dual-channel digital quadrature lock-in amplifier (DLIA) is used to measure the 2^{nd} harmonic signals for gas concentration calculation, the bandwidth of the 8-order lowpass filter of the DLIA is set to 1 Hz to reduce noise interference. To realize simultaneous detection of dual gases CH_4/CO_2, the system operates in FDM mode, in another word, two DFB lasers are modulated in different frequencies $f_1/2$ and $f_2/2$, then the absorption-induced 2^{nd} harmonic signals in frequency of f_1 and f_2 can be separated by the DLIA to identify CH_4 or CO_2. Sample gases used in the experiments are provided by a gas mixing system as shown in Fig. 5, including three flowmeters, 99.999% pure nitrogen, 1% CH_4, 0.05% CH_4 and 1% CO_2.

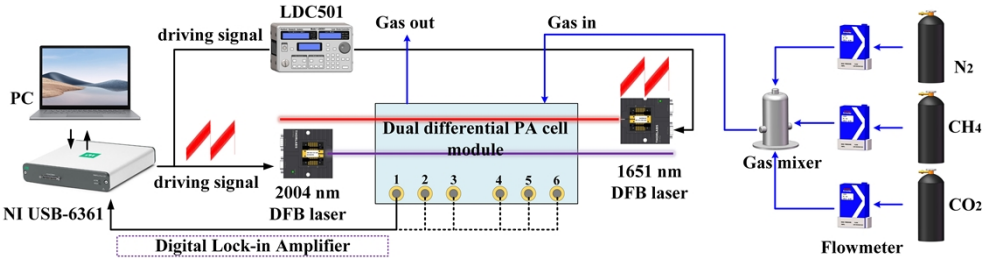

Fig. 5. Schematic of the experiment system. 1: microphone-1output, 2: microphone-2 output, 3: differential-1 output, 4: microphone-3 output, 5: microphone-4 output, 6: differential-2 output.

Optics EXPRESS

4. Experiment results

4.1. Measured frequency response of the differential PA cell

Frequency response of the developed differential PA cell has been simulated in section 2.2 as displayed in Fig. 2(b), the first step of our experiment is to measure the frequency response curve of the manufactured PA cell. A CH_4 concentration of 200 ppm is used in this measurement, the frequency response curve of each resonator is measured respectively as plotted in Fig. 6(a, b). In addition, frequency response of the differential output is also measured as shown in Fig. 6(c). The results indicate that the resonant frequency of the fabricated PA cell is near 3100.3 Hz, which is slightly different from the simulated result of 3124 Hz. Nonlinear fitting utilizing a Lorentzian profile is performed on the frequency response data, the full width at half maximum (FWHM) is determined to be ~163 Hz, resulting in a Q-factor of 19. Such difference between experiment and simulation may arise from fabrication errors of PA cell and test conditions.

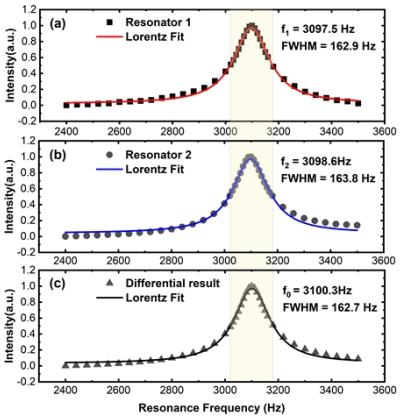

Fig. 6. Frequency response of the differential PA cell. (a) Frequency response of resonator 1, (b) Frequency response of resonator 2, (c) Frequency response of differential output.

4.2. Photoacoustic signal enhancement by the DD-PAS

In this section, we pay attention to discuss the photoacoustic signal enhancement by the DD-PAS. Concentration of 200 ppm CH_4 gas sample is still used to measure the absorption-induced 2nd harmonic signal for comparison. The signals of the four microphones and their differential counterparts are detected in the same condition and compared in Fig. 7(a, b). The 1 σ standard deviation is calculated based on the non-absorption baseline to evaluate the SNR. Comparing the photoacoustic signals between Mic-1 and Mic-2, Mic-3 and Mic-4, we find that the acoustic strength in resonator-1 is a little stronger than resonator-2.

$$V_{out} = \underbrace{(Mic\_1 - Mic\_2)}_{Diff1} + \underbrace{(Mic\_3 - Mic\_4)}_{Diff2} \quad (1)$$

Differential process between Mic-1 and Mic-2, Mic-3 and Mic-4 as Eq. (a) almost doubles the photoacoustic signal, meanwhile reducing the noise level. Common-mode noise is significantly eliminated by the differential operation, as a result, the SNR is improved by 7~8 times. As to dual differential strategy, two differential results Diff-1 and Diff-2 are added up first and then for 2nd harmonic detection to further increase the photoacoustic signal as shown in Fig. 7(c), however, the noise level is not worsened too much. In a word, the dual differential method based on four microphones can effectively increase the photoacoustic signal compared with a

Optics EXPRESS

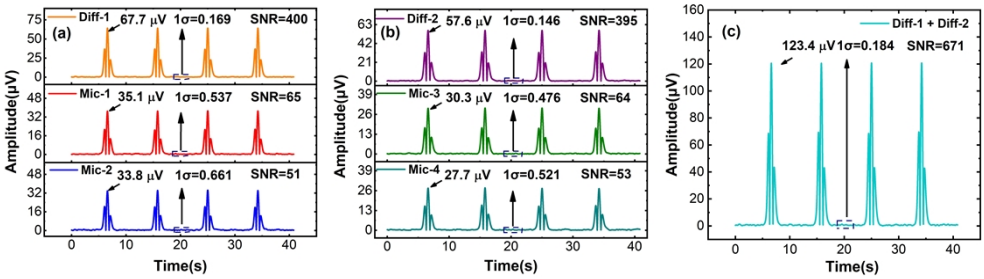

Fig. 7. Verification of DD-PAS for photoacoustic signal enhancement based on 200 ppm CH_4 gas. (a) The Mic-1, Mic-2 and differential photoacoustic signal from first circuit board. (b) The Mic-3, Mic-4 and differential photoacoustic signal from second circuit board. (c) Photoacoustic signal of Diff1 + Diff2.

single microphone, moreover it successfully improves the SNR by > 10 times. In the following experiments, the dual differential output is used as the Eq. (1) for concentration measurement.

4.3. *Dual gas CH_4/CO_2 detection*

To realize simultaneous detection of dual gases CH_4 and CO_2, FDM technique was employed to drive the 1651 nm and 2004nm lasers. Fourier transform analysis was performed to determine the respective modulation frequencies $f_1/2$ and $f_2/2$ of two lasers. In the experiment, high concentration CH_4 and CO_2 were mixed in the PA cell, the dual differential signal V_{out} as mentioned in section 4.2 was collected by DAQ card for Fourier transform analysis as shown in Fig. 8. In the very beginning, the modulation frequencies of two DFB lasers were set to 1549 Hz and 1551 Hz, as a result, their 2nd harmonic signals were so close that it was difficult to separate by filtering as plotted in Fig. 8(a). Thus, we further increased the distance between $f_1/2$ and $f_2/2$ to 1547 Hz and 1553 Hz as displayed in Fig. 8(b), their corresponding 2nd harmonic components gradually left apart from each other, but were still very close. We continuously adjusted the $f_1/2$ and $f_2/2$ to 1545 Hz and 1555 Hz, their absorption-induced 2nd harmonic components (3090 Hz and 3110 Hz) were obviously separated by 20 Hz distance as shown in Fig. 8(c), which gave our confidence that it was very easy to separate the CH_4 signal and CO_2 signal by the 1 Hz bandwidth filter of DLIA. Meanwhile, considering the wide frequency response curve of the PA cell as measured in Fig. 2, the signal amplitude did not decline too much even the operating frequency was set apart from the center frequency of 3100.3 Hz by 10 Hz. As estimated based on the Lorentz fit in Fig. 6, only 1% of amplitude loss was measured compared with the resonance center. Thus, in the following experiments, 1545 Hz was used to modulate the 1651 nm laser for CH_4 detection and 1555 Hz was used to modulate the 2004nm laser for CO_2 detection.

Given that WMS technique was adopted in the DD-PAS system, optimization experiment was carried out to determine the optimal modulation amplitudes for 1651 nm and 2004nm lasers. In the experiment, 1% CH_4 and 0.2% CO_2 were provided and kept constant respectively to optimize the modulation amplitude. The measured 2nd harmonic amplitudes versus different modulation amplitudes in current unit were plotted in Fig. 9, the optimal modulation amplitude was 7 mA for 1651 nm laser to reach the maximum 2nd harmonic value for CH_4 detection. For the CO_2 detection channel, the modulation amplitude should be set at 3.75 mA as shown in Fig. 9(b). Thus, the optimized modulation amplitudes were determined and used in the following experiments.

After the above section of pre-experiments, the key parameters of the DD-PAS system have been fixed, including the sawtooth scanning frequency (0.1 Hz), wavelength modulation frequency (1545 Hz for CH_4 detection, 1555 Hz for CO_2 detection), lowpass bandwidth of DLIA (8-order 1 Hz), laser driving current modulation amplitude (7 mA for 1651 nm laser and 3.75 mA for

Optics EXPRESS

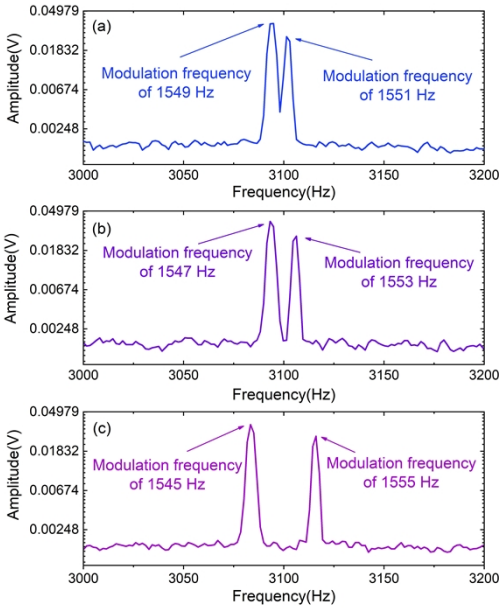

Fig. 8. Verification of the FDM working mode to determine the modulation frequency $f_1/2$ and $f_2/2$. (a) $f_1/2 = 1549$ Hz and $f_2/2 = 1551$ Hz, (b) $f_1/2 = 1547$ Hz and $f_2/2 = 1553$ Hz, (c) $f_1/2 = 1545$ Hz and $f_2/2 = 1555$ Hz.

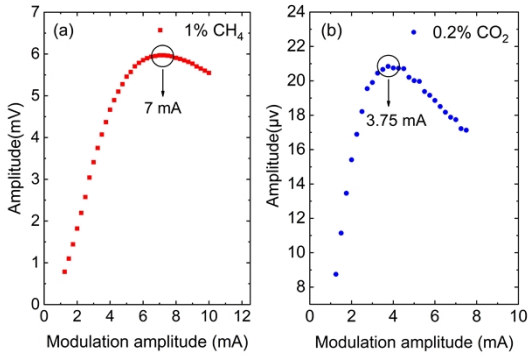

Fig. 9. The modulation amplitude optimization experiment. (a) Modulation amplitude optimized results for CH_4 detection, (b) Modulation amplitude optimized results for CO_2 detection.

2004nm laser). Afterwards, sample CH_4 in different concentrations from 10 ppm to 500 ppm and sample CO_2 in different concentrations from 400 ppm to 5000 ppm were provided by the gas mixing system for dual gases detection test. The measured 2nd harmonic curves of different concentrations CH_4 were displayed in Fig. 10(a), the corresponding amplitudes were measured and plotted as shown in Fig. 10(b), based on which linear fitting was performed to achieve an efficiency of 0.62 uV/ppm with an R^2 of 0.9998. For CO_2 detection channel, 2nd harmonic curves of different concentrations CO_2 were displayed in Fig. 10(c), the corresponding amplitudes were measured and plotted in Fig. 10(d), linear fitting was performed as well to achieve an efficiency of 0.01 uV/ppm with an R^2 of 0.9999.

To evaluate the sensitivity for CH_4 and CO_2 detection of the DD-PAS system, a long-term experiment of 2-3 hours was carried out for Allan deviation analysis. In the long-term experiment,

Optics EXPRESS

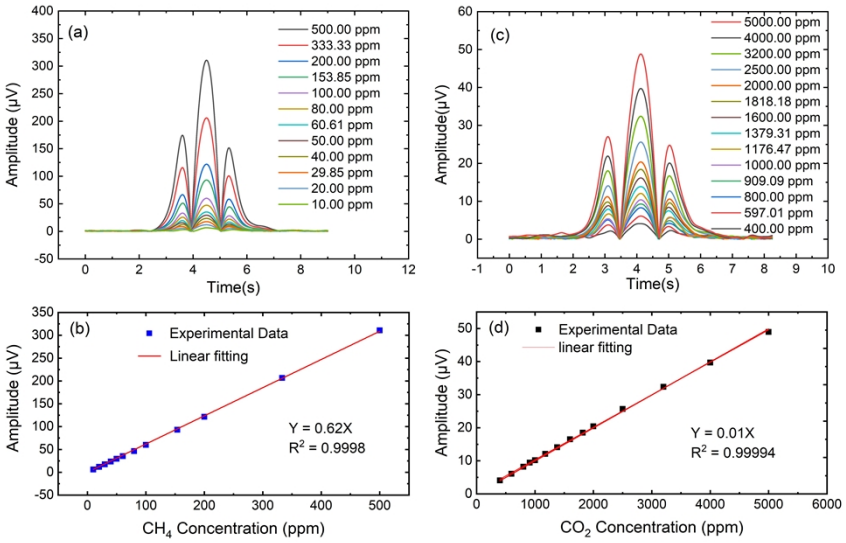

Fig. 10. Linear test of in different gas concentrations. (a) Second harmonic curves of different CH_4 concentrations, (b) Linear fitting of measured CH_4 results, (c) Second harmonic curves of different CO_2 concentrations, (b) Linear fitting of measured CO_2 results.

20 ppm CH_4 and 1000 ppm CO_2 sample gases were provided for measurement, the 2nd harmonic amplitudes were measured and saved at a sampling rate of one data point per ten seconds, by the way the measured amplitudes in voltage were converted into concentration unit as shown in Fig. 11(a, c). Based on the saved data in 2-3 hours, Allan deviation analysis was applied to evaluate the potential detection sensitivity when we increased the integration time. For the CH_4 detection channel, a detection sensitivity of 0.44 ppm was achieved at an integration time of 10 s, and the sensitivity would be further improved to 0.14 ppm at 100 s integration time and 42 ppb at 1000 s integration time as displayed in Fig. 11(b). Considering that 1651 nm laser output at CH_4 absorption center was estimated to be ~30 mW, the best power-normalized noise equivalent absorption (NNEA) was calculated to be 4.7 $\times 10^{-10} cm^{-1} WHz^{-1/2}$) for CH_4 detection. For the CO_2 detection channel, a detection sensitivity of 7.39 ppm was achieved at an integration time of 10 s, and the sensitivity would be further improved to 2.34 ppm at 100 s integration time and 0.86 ppm at 1000 s integration time as displayed in Fig. 11(d). The best NNEA for CO2 detection was calculated to be 5.3 $\times 10^{-10} cm^{-1} WHz^{-1/2}$. So, the best detection sensitivity of both CH_4 and CO_2 can be realized at a sub-ppm level and a NNEA of $10^{-10} cm^{-1} WHz^{-1/2}$ by the proposed DD-PAS system.

As to the minimum detection limit (MDL), the 2nd harmonic amplitudes were continuously measured over 2 hours in 99.999% nitrogen and saved as shown in Fig. 12. Statistic analysis was performed on the measured data in Fig. 12 to calculate the mean value, and used the mean value to represent the non-absorption background of the DD-PAS system. Results in Fig. 12 indicate that the background of CH_4 and CO_2 channels are both 0.6 μV, which cannot be reduced any more by increasing the integration time. Furthermore, we repeatedly measured the background for several times which indicated that the mean value was very stable at 0.6 μV. So, any absorption-induced photoacoustic signal below 0.6 μV cannot be identified any more. We substitute 0.6 μV to the linear fitted equations in Fig. 10(b, d) respectively to determine the MDL of CH_4 and CO_2 channels. The MDL for CH_4 detection is estimated to be 0.97 ppm and the MDL for CO_2 detection is estimated to be 60 ppm. It was also informed in Fig. 12 that the background dispersion of CH_4 channel was larger than CO_2 channel. The reason may be that a higher power

Optics EXPRESS

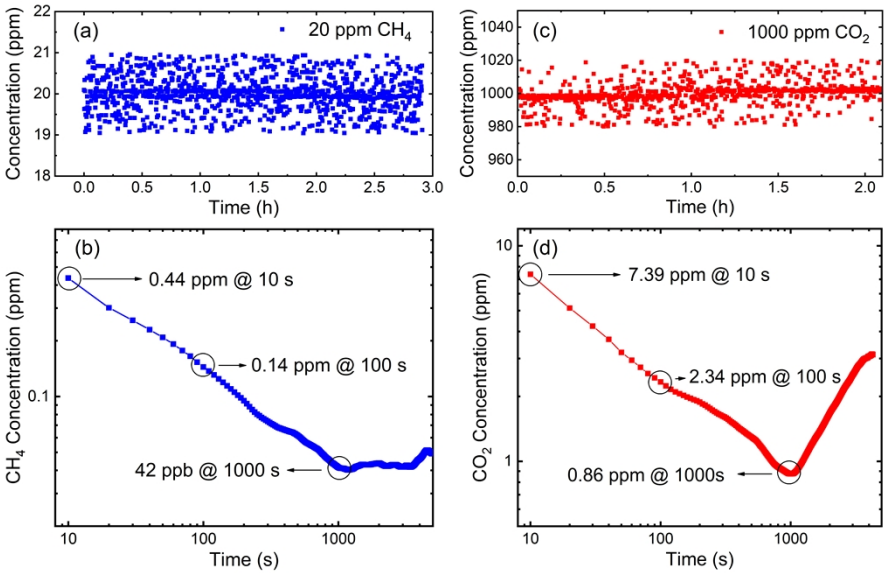

Fig. 11. Allan deviation analysis to evaluate the sensitivity. (a) The long-term measured results of 20 ppm CH_4, (b) The Allan deviation analysis for CH_4 detection sensitivity, (c) The long-term measured results of 1000 ppm CO_2, (d) The Allan deviation analysis for CO_2 detection sensitivity.

1651 nm laser was used for CH_4 detection than the 2004nm laser, higher optical power induced additional noise.

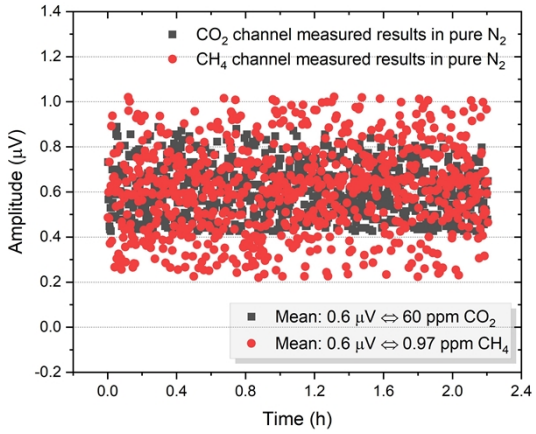

Fig. 12. Minimum detection limit analysis for CH_4 and CO_2, non-absorption background measured in 99.999% nitrogen.

In the end, the developed dual gas DD-PAS system was used to monitor the CH_4 and CO_2 concentrations in our laboratory from 6:00 am to 9:00 pm. The measured results are displayed in Fig. 13. In the very beginning, the lab space CH_4 is measured to be 1.7 ppm, which is very close to the current atmospheric CH_4 concentration of 1.8~1.9 ppm according to data released in January 2022 by the US National Oceanic and Atmospheric Administration (NOAA) [41]. During the monitoring period, we mixed different concentrations of CH_4 to release into the

Optics EXPRESS

lab space to simulate CH_4 leakage as shown in Fig. 13(a), and to verify if the DD-PAS would sense the leakage accident. Good news is that sub-ppm changes coming from only 100 ppm CH_4 leakage can be easily caught as depicted in Fig. 13(a) around 7:00. Furthermore, different degrees of leakage can be identified as well when observing the leakage accidents around 12:00. In addition, the atmospheric CH_4 concentration keeps rising, from 1.7 ppm to 2.2 ppm, 2.4 ppm and 2.7 ppm in the end, as we continuously emitting CH_4 gas into the lab space during the experiment. So, high sensitivity of the CH_4 detection channel has been verified by the long-term monitoring experiment. As to the CO_2 detection channel, the monitored results also reflect the daily changes in CO_2 concentration in the laboratory. In the morning of 7:00, the CO_2 concentration drops when we open the window to inlet the fresh air into lab space. Afterwards, the CO_2 concentration increases as more and more students coming to the laboratory for experiments. During the lunch and dinner time, the CO_2 concentration decreases because of students leaving the laboratory. In a word, the CO_2 concentration is closely related to the activities of personnel in the laboratory.

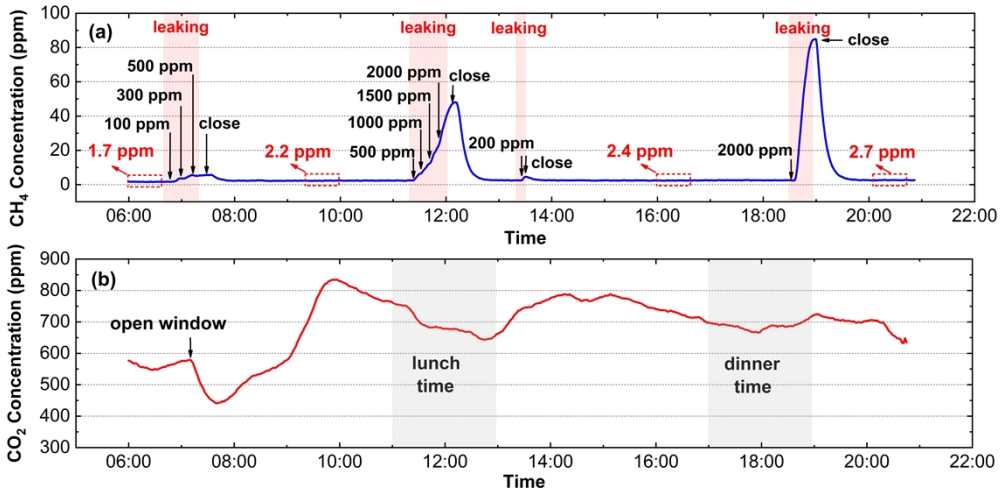

Fig. 13. Long-term atmospheric CH_4 and CO_2 monitoring within the laboratory from 6:00 to 21:00.

Considering that the water bodies, including ocean, lake, river and artificial reservoir, absorb a large amount of greenhouse gases, which is crucial for regulating the greenhouse effect. We take this as a goal that expanding the PAS technique for greenhouse gases monitoring from gas phase space to liquid phase detection in this study. In the first step, we designed a dual-differential PAS cell and improved it to a small inner volume, based on which a DD-PAS system was developed to measure the two main greenhouse gases, methane and carbon dioxide. Even the detection sensitivity has reached the sub-ppm level after experimental evaluation. However, the NOAA's analysis showed that the average annual increases in atmospheric CH_4 and CO_2 concentrations are only tens of ppb and a few ppm respectively, which is a very small amount. Therefore, detection sensitivity of the proposed DD-PAS system should be further improved to ppb level in our opinion which is our next research plan. Afterwards, the DD-PAS system can be integrated in a waterproofed pressure cabin to measure the dissolved CH_4 and CO_2 in water surface and deep sea. By virtue of the advantage of low gas consumption from PAS technique, we expect to increase the response speed of current dissolved gas detection instruments limited by the membrane degassing efficiency. The measured data can serve as a supplement to space greenhouse gases monitoring. In other applications with low requirements for sensitivity and MDL, such as CH_4 leakage detection, indoor monitoring and so on, the developed DD-PAS system can serve as a good sensor for trace gas detection.

Optics EXPRESS

5. Conclusion

In this study, differential PA cell is re-designed by reducing the volumes of resonators and buffer chambers, compressing the gas consumption to a level of < 8 mL to meet the potential requirement of dissolved gas detection. Meanwhile, a dual differential strategy is proposed to increase the photoacoustic signal and system SNR, as a result, the photoacoustic amplitude is increased by 4 times and the SNR is improved by an order of magnitude compared with single-microphone-based PA cell. Compared with optical methods frequently used to enhance the photoacoustic signal, for example the intra-cavity and extra-cavity methods, the dual differential strategy is easier for implementation without complex optical alignment. In addition, FDM technique is employed to realize the dual gases detection in this study. Benefiting from the wide FWHM of frequency-response curve of PA cell, more gases can be simultaneously measured based on the FDM technique other than dual gases detection.

To improve the performance of the DD-PAS system, noise level is expected be reduced and photoacoustic signal should be further enhanced. Based on our analysis and operating experience during the experiments, the background noise within the lock-in bandwidth of the differential circuit itself is only ~ 0.1 μV, the window-absorption-induced noise has been eliminated by differential operation. We conclude that most of the noise comes from the microphones. We can test more brands of microphones and choose the best one with lowest noise, or develop new acoustic sensor to improve the noise level. To enhance the photoacoustic strength, more efficient photoacoustic enhanced structures can be studied, and higher power excitation laser source is required. For example, Tm^{3+}-doped fiber can be used to amplify the laser power at 2 μm to enhance the photoacoustic signal for CO_2 detection and Raman fiber can be used to amplify the laser power at 1651 nm to enhance the photoacoustic signal of CH_4 channel. Of course, such approach would increase the complexity of PAS system. In the following study, we will further improve the DD-PAS according to the above research plan to realize multiple gases detection, higher detection sensitivity and lower MDL.

Funding. National Natural Science Foundation of China (52001295, 62005267, 62375262); Natural Science Foundation of Shandong Province (ZR2020QF097); Open Fund of State Key Laboratory of Applied Optics (SKLAO2021001A12).

Disclosures. The authors declare no conflicts of interest.

Data availability. Data presented in this paper are not publicly available at this time but may be obtained from the authors upon reasonable request.

References

1. Intergovernmental Panel on Climate Change, https://www.ipcc.ch.
2. S. Kirschke, P. Bousquet, and P. Ciais, *et al.*, "Three decades of global methane sources and sinks," Nat. Geosci. **6**(10), 813–823 (2013).
3. D. J. Wuebbles and K. Hayhoe, "Atmospheric methane and global change," Earth-Sci. Rev. **57**(3-4), 177–210 (2002).
4. D. Bastviken, L. J. Tranvik, J. A. Downing, P. M. Crill, and A. Enrich-Prast, "Freshwater methane emissions offset the continental carbon sink," Science **331**(6013), 50 (2011).
5. R. K. Thauer, A. K. Kaster, H. Seedorf, W. Buckel, and R. Hedderich, "Methanogenic archaea: ecologically relevant differences in energy conservation," Nat. Rev. Microbiol. **6**(8), 579–591 (2008).
6. A. Sepulveda-Jauregui, K. Karla Martinez-Cruz, A. Strohm, K. M. W. Anthony, and F. Thalasso, "A new method for field measurement of dissolved methane in water using infrared tunable diode laser absorption spectroscopy," Limnol. Oceanogr. Meth. **10**(7), 560–567 (2012).
7. R. Wang and L. Guo, "The distribution of combustible ice and the status of exploitation," IOP Conf. Ser.: Earth Environ. Sci. **467**(1), 012069 (2020).
8. R. A. Dawe and S. Thomas, "A large potential methane source—Natural gas hydrates," Energy Sources Part A-Recovery Util. Environ. Eff. **29**(3), 217–229 (2007).
9. J. W. Swinnerton, V. J. Linnenbom, and C. H. Cheek, "Determination of Dissolved Gases in Aqueous Solutions by Gas Chromatography," Anal. Chem. **34**(4), 483–485 (1962).
10. M. M. R. Jahangir, P. Johnston, M. I. Khalil, J. Grant, C. Somers, and K. G. Richards, "Evaluation of headspace equilibration methods for quantifying greenhouse gases in groundwater," J. Environ. Manage. **111**, 208–212 (2012).
11. M. Schlüter and T. Gentz, "Application of membrane inlet mass spectrometry for online and in situ analysis of methane in aquatic environments," J. Am. Soc. Mass Spectrom. **19**(10), 1395–1402 (2008).

Optics EXPRESS

12. R. J. Bell, J. Ryan, R. T. Short, F. H. W. Van Amerom, and R. H. Byrne, "Calibration of an in-situ membrane inlet mass spectrometer for measurements of dissolved gases and volatile organics in seawater," Environ. Sci. Technol. **41**(23), 8123–8128 (2007).
13. E. R. Crosson, "A cavity ring-down analyzer for measuring atmospheric levels of methane, carbon dioxide, and water vapor," Appl. Phys. B **92**(3), 403–408 (2008).
14. X. Li, X. Fan, Y. He, B. Chen, L. Yao, M. Hu, and R. Kan, "Development of a compact tunable diode laser absorption spectroscopy-based system for continuous measurements of dissolved carbon dioxide in seawater," Rev. Sci. Instrum. **90**(6), 065110 (2019).
15. Z. Liu, C. Zhang, T. Zhang, Y. Zhang, and F. K. Tittel, "High-precision methane isotopic abundance analysis using near-infrared absorption spectroscopy at 100 Torr," Analyst **146**(2), 698–705 (2021).
16. R. Gonzalez-Valencia, F. Magana-Rodriguez, O. Gerardo-Nieto, A. Sepulveda-Jauregui, K. Martinez-Cruz, K. Walter Anthony, D. Baer, and F. Thalasso, "In situ measurement of dissolved methane and carbon dioxide in freshwater ecosystems by off-axis integrated cavity output spectroscopy," Environ. Sci. Technol. **48**(19), 11421–11428 (2014).
17. Z. Liu, C. Zheng, T. Zhang, Y. Li, Q. Ren, C. Chen, W. Ye, Y. Zhang, Y. Wang, and F. K. Tillel, "Midinfrared Sensor system based on tunable laser absorption spectroscopy for dissolved carbon dioxide analysis in the South China Sea: System-level integration and deployment," Anal. Chem. **92**(12), 8178–8185 (2020).
18. Z. Liu, C. Zheng, C. Chen, Y. Li, H. Xie, Q. Ren, Y. Wang, and F. K. Tittel, "ICL-based mid-infrared carbon dioxide sensor system for deep-sea natural gas hydrate exploration," Opt. Express **27**(4), 5598–5609 (2019).
19. H. M. Roberts and A. M. Shiller, "Determination of dissolved methane in natural waters using headspace analysis with cavity ring-down spectroscopy," Anal. Chim. Acta **856**, 68–73 (2015).
20. M. Hu, B. Chen, L. Yao, C. Yang, X. Chen, and R. Kan, "A Fiber-Integrated CRDS Sensor for In-Situ Measurement of Dissolved Carbon Dioxide in Seawater," Sensors **21**(19), 6436 (2021).
21. F. Yuan, M. Hu, Y. He, B. Chen, L. Yao, Z. Xu, and R. Kan, "Development of an in-situ analysis system for methane dissolved in seawater based on cavity ringdown spectroscopy," Rev. Sci. Instrum **91**(8), 083106 (2020).
22. F. Wang, Y. Cheng, Q. Xue, Q. Wang, R. Liang, J. Wu, J. Sun, C. Zhu, and Q. Li, "Techniques to enhance the photoacoustic signal for trace gas sensing: A review," Sens. Actuator A-Phys **345**, 113807 (2022).
23. X. Mao, X. Zhou, L. Zhai, and Q. Yu, "Dissolved Gas-in-Oil Analysis in Transformers Based on Near-Infrared Photoacoustic Spectroscopy," Int J Thermophys **36**(5-6), 940–946 (2015).
24. C. Li, H Qi, X. Zhao, M. Guo, R. An, and K. Chen, "Multi-pass absorption enhanced photoacoustic spectrometer based on combined light sources for dissolved gas analysis in oil," Opt. Lasers Eng **159**, 107221 (2022).
25. C. Li, K. Chen, J. Zhao, H. Qi, X. Zhao, F. Ma, X. Han, M. Guo, and R. An, "High-sensitivity dynamic analysis of dissolved gas in oil based on differential photoacoustic cell," Opt. Lasers Eng **161**, 107394 (2023).
26. G. Wang, D. Fu, S. Yuan, C. Li, X. Han, J. Du, F. Du, and K. Chen, "Rapid detection of dissolved acetylene in oil based on T-type photoacoustic cell," Microw. Opt. Technol. Lett (2023).
27. F. Wang, Q. Xue, J. Chang, Z. Wang, J. Sun, X. Luan, and C. Li, "Wavelength scanning Q-switched fiber-ring laser intra-cavity QEPAS using a standard 32.76 kHz quartz tuning fork for acetylene detection," Opt. Laser Technol **134**, 106612 (2021).
28. Y. Ma, T. Liang, S. Qiao, X. Liu, and Z. Lang, "Highly Sensitive and fast hydrogen detection based on light-induced thermoelastic spectroscopy," Ultrafast Sci **3**, 0024 (2023).
29. W. Chen, S. Qiao, Z. Lang, J. Jiang, Y. He, Y. Shi, and Y. Ma, "Hollow-waveguide-based light-induced thermoelastic spectroscopy sensing," Opt. Lett. **48**(15), 3989–3992 (2023).
30. Z. Lang, S. Qiao, and Y. Ma, "Fabry–Perot-based phase demodulation of heterodyne light-induced thermoelastic spectroscopy," Light: Advanced Manufacturing **4**(2), 1 (2023).
31. Y. Liu, H. Lin, BAZ. Montano, W. Zhu, Y. Zhong, R. Kan, B. Yuan, J. Yu, M. Shao, and H. Zheng, "Integrated near-infrared QEPAS sensor based on a 28 kHz quartz tuning fork for online monitoring of CO2 in the greenhouse," Photoacoustics **25**, 100332 (2022).
32. H. Zhao, H. Zhang, M. Hu, M. Hu, Y. Zhou, J. Liang, and Q. Wang, "A Fiber-Coupled Quartz-Enhanced Photoacoustic Sensor for Dissolved Gas Detection," Photonics **10**(2), 127 (2023).
33. F. Wang, J. Chang, Q. Zhang, Z. Qin, and C. Zhu, "Pivotal techniques evaluation in QEPAS system for engineering applications," Measurement **135**, 376–384 (2019).
34. Z. Li, J. Liu, G. Si, Z. Ning, and Y. Fang, "Design of a high-sensitivity differential Helmholtz photoacoustic cell and its application in methane detection," Opt. Express **30**(16), 28984–28996 (2022).
35. C. Zhang, S. Qiao, Y. He, S. Zhou, L. Qi, and Y. Ma, "Differential quartz-enhanced photoacoustic spectroscopy," Appl. Phys. Lett. **122**(24), 241103 (2023).
36. Z. Li, J. Liu, G. Si, Z. Ning, and Y. Fang, "Active noise reduction for a differential Helmholtz photoacoustic sensor excited by an intensity-modulated light source," Opt. Express **31**(2), 1154–1166 (2023).
37. Q. Wang, Z. Wang, J. Chang, and W. Ren, "Fiber-ring laser-based intracavity photoacoustic spectroscopy for trace gas sensing," Opt. Lett. **42**(11), 2114–2117 (2017).
38. X. Yin, L. Dong, H. Wu, H. Zheng, W. Ma, L. Zhang, W. Yin, S. Jia, and FK. Tittel, "Sub-ppb nitrogen dioxide detection with a large linear dynamic range by use of a differential photoacoustic cell and a 3.5 W blue multimode diode laser," Sens. Actuator B-Chem **247**, 329–335 (2017).
39. C. Zhang, S. Qiao, and Y. Ma, "Highly sensitive photoacoustic acetylene detection based on differential photoacoustic cell with retro-reflection-cavity," Photoacoustics **30**, 100467 (2023).

Optics EXPRESS

40. F. Wang, R. Liang, Q. Xue, Q. Wang, J. Wu, Y. Cheng, J. Sun, and Q. Li, "A novel wavelength modulation spectroscopy gas sensing technique with an ultra-compressed wavelength scanning bandwidth," Spectroc. Acta Pt. A-Molec. Biomolec. Spectr. **280**, 121561 (2022).
41. https://www.noaa.gov/news-release/increase-in-atmospheric-methane-set-another-record-during-2021.